

Supplementary Materials for

Achieving higher photoabsorption than group III-V semiconductors in ultra-fast thin silicon photodetectors with integrated photon-trapping surface structures

Wayesh Qarony^{1†}, Ahmed S. Mayet^{1†}, Ekaterina Ponizovskaya Devine², Soroush Ghandiparsi¹, Cesar Bartolo-Perez¹, Ahasan Ahamed¹, Amita Rawat¹, Hasina H. Mamtaz¹, Toshishige Yamada^{2,3}, Shih-Yuan Wang², M. Saif Islam^{1*}

¹Electrical and Computer Engineering, University of California—Davis; Davis, CA 95618, USA.

²W&WSens Devices, Inc., 4546 El Camino; Los Altos, CA 94022, USA.

³Electrical and Computer Engineering, Baskin School of Engineering; University of California, Santa Cruz, CA 95064, USA.

† These authors contributed equally to this work

*Corresponding author. Email: sislam@ucdavis.edu

This PDF file includes:

Supplementary Text
Figs. S1 to S11
Tables S1
Captions for Movies S1 to S3
References

Other Supplementary Materials for this manuscript include the following:

Movies S1 to S3

1 Fabrication of photodetectors

The Si absorber layer (*p*-type) with a thickness of 1000 nm was epitaxially grown on a silicon-on-insulator (SOI) substrate. The SOI wafer has a 1000 nm buried oxide layer BOX, where the active layer was epitaxially grown with a resistivity of 14-22 ohm-cm. Next, the native oxide was removed by cleaning the surface of the Si with buffered oxide etching BOE (6:1) process. The fabrication process flow chart is shown in Fig. S1, while the detailed process steps are described in the following.

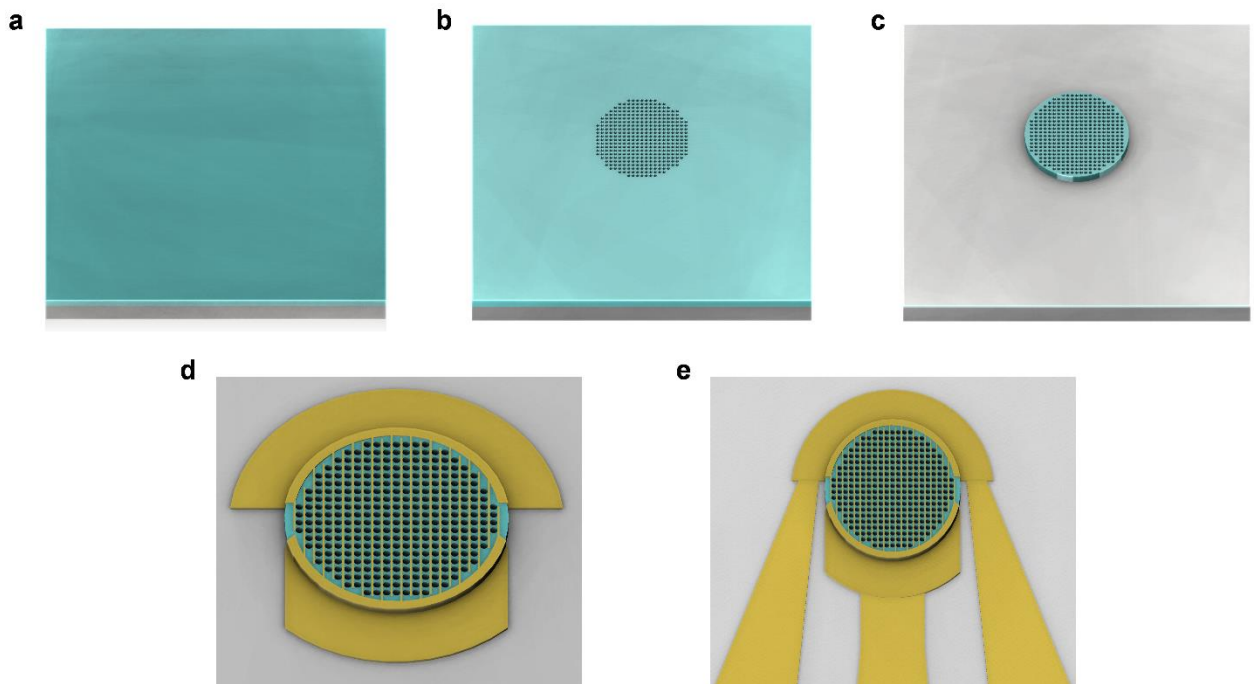


Figure S1: **Flow chart of the fabrication process of Si metal-semiconductor-metal photon-trapping photodetectors devices.** (a) Epitaxially grown *p*-type 1000 nm thick silicon on SiO₂ SOI wafer. (SOI wafer substrate: Gray (SiO₂), epitaxially grown Si: Turquoise (Si)). The native oxide of the wafer is cleaned by the buffered oxide etching BOE (6:1) process. (b) Photon-trapping holes patterning using DUV photolithography and DRIE holes etching. (c) Mesa etches to the substrate layer (SiO₂). (d) 100 nm thick, and 300 nm width interdigitated aluminum (Al)

metals sputtered and lift-off to form Schottky contact: Gold (interdigitated Schottky contact). (e)
Coplanar waveguide metal deposition (CPW: Gold).

1.1 Photon-trapping hole formation

Right after the wafer cleaning, sub-micron photon-trapping (PT) hole arrays were patterned using a stepper lithography system. In the stepper system, we can adjust the focus of the ultraviolet (UV) light to shrink the features present on the mask plate and enables sub-micron feature patterning. Next, PT hole arrays were etched in a reactive ion etching (RIE) process. Fluorine-based chemistry was utilized to etch holes in the silicon. The fabricated PT structures possess a period, diameter, and hole depth of 1300, 1000, and 600 nm, respectively.

1.2 Mesa isolation

In this process step, the top and the bottom mesa structures of the photodetector were patterned. The top mesa was defined followed by the bottom mesa in alignment with the previously patterned PT structures by utilizing the stepper and RIE system. Patterning the top mesa exposes the bottom contact layer on the stack, whereas the bottom mesa patterning isolates the photodetectors from the neighboring devices.

1.3 Metallization

In the next step, the Si substrate was cleaned with BOE (6:1) to remove the native oxide before the metal deposition. The interdigitated aluminum (Al) fingers with a thickness of 100 nm and width of 300 nm were sputtered on the Si in an RF sputter system. Uniform Schottky contacts were prepared by lifting off the sputtered Al.

1.4 Co-planner waveguide patterning

After the metallization, the sample was patterned for co-planar waveguide contact. In this step, about 300 nm of Al layer was deposited followed by a lift-off process to create coplanar waveguides (CPW), which utilizes for the high-speed transport of the electrical pulse converted from a picosecond (ps) pulsed laser by the fabricated photodetectors.

1.5 Passivation

The passivation process step is conducted after completing the fabrication of the devices. To passivate the surface states created on the sidewalls of the holes and mesa, 2% HF was used for 3 seconds with HF:H₂O, 1:100 ratio. The hydrogen ion present in the solution attaches itself to the surfaces and neutralizes the active surface state. This passivation process reduces the dark state leakage current.

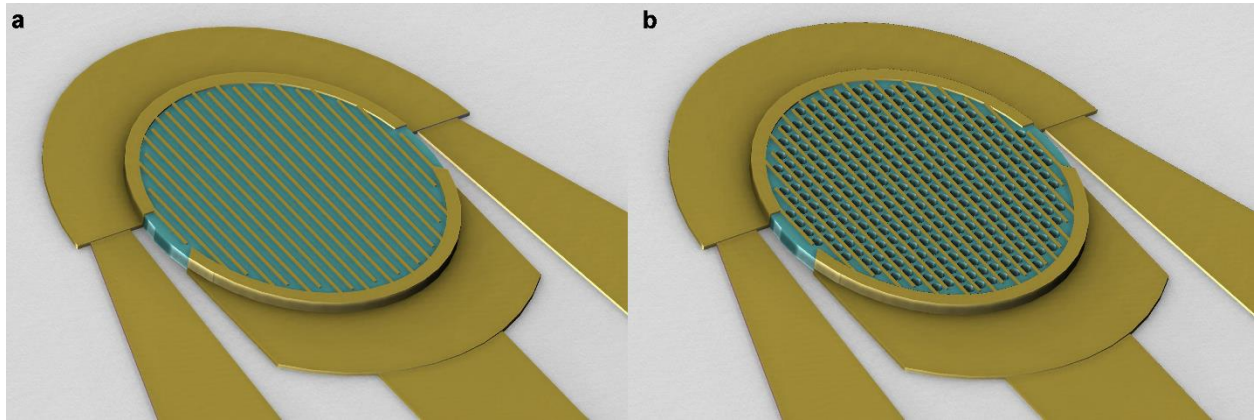


Figure S2: **Schematic of Si MSM fabricated photodetector devices.** (a) Planar (flat) surface, (b) Photon trapping Si MSM photodetector.

Metal semiconductor metal or MSM control photodetectors without integrated PT structures were also fabricated to compare their performance with the PT MSM photodetectors. The schematics of both control and PT photodetectors are shown in Fig. S2, while the optical

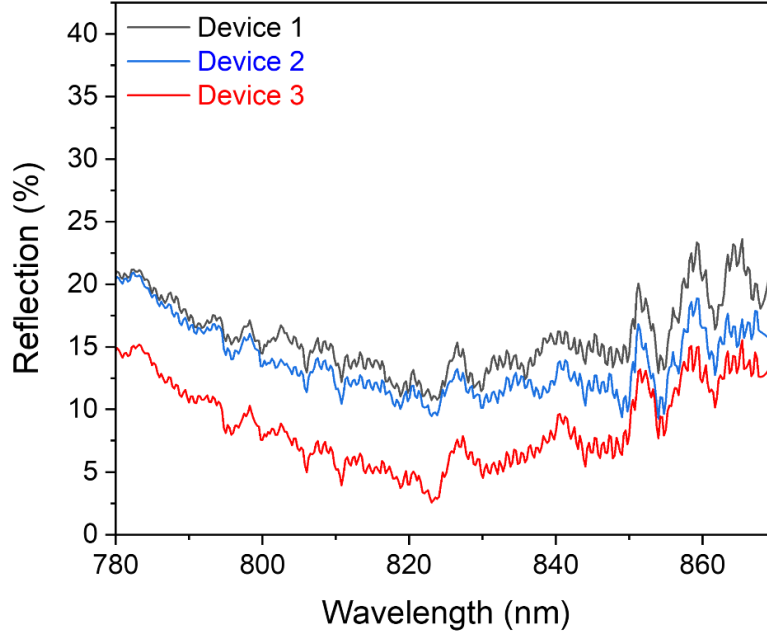


Figure S4: **Measured reflection characteristics of photon-trapping devices by varying the diameter and periodicity of holes.**

2. Simulation methods

A 3D finite-difference time-domain (FDTD) optical simulation was utilized to rigorously solve Maxwell's curl equations to calculate the electromagnetic (EM) fields within the photodetectors. The simulations were performed for the array of cylindrical holes of 700 nm diameter with a 1000 nm period in Si slab of 1000 nm thin on SiO₂ substrate. The depth of the holes was assumed to be 1000 nm. Furthermore, the optical absorption in Si was approximated by the Lorentz model with parameters fitted to the data at the range of around 850 nm wavelength. In FDTD, the incident pulse had a Gaussian-shaped spectrum between 600 to 1200 nm, spatially it is a plane wave. The averaged amplitude vs. wavelengths of the signal that were reflected and transmitted at the bottom and the sides were detected using Fourier transform. Then the reflected (R) and transmitted (T)

power normalized to the input source were calculated. The absorption (A) was calculated as $A = I - R - T$. Boundary conditions in the direction of light propagation were assumed to be Perfectly Matched Layers (PML). Periodical boundary conditions were considered for the other directions around the simulation area.

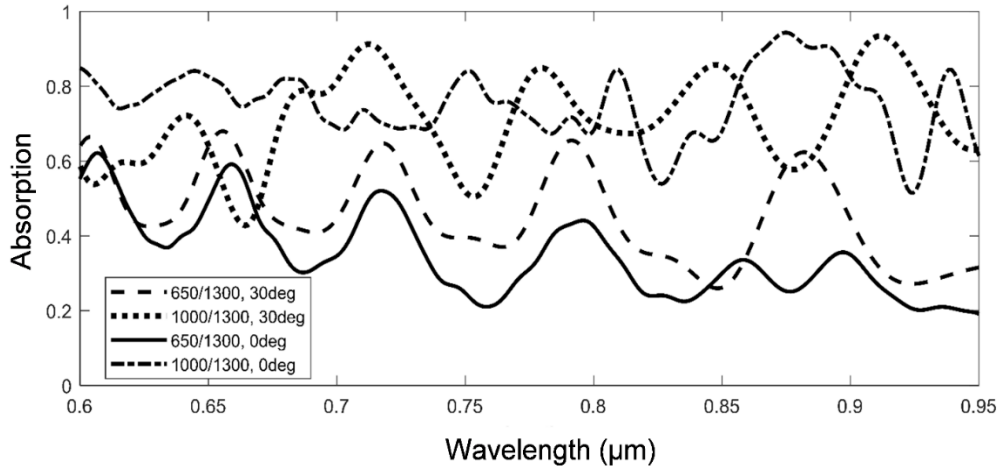


Figure S5: Photon absorption in photodetectors with small and large holes under different illumination angles. Effect of coupling phenomena for small and large holes at different incident angles of light on the photon absorption in Si photon-trapping photodetectors.

Fig. S6 estimates optical losses caused by the interdigitated metal on top of the MSM planar (Fig. S6(a)) and photon-trapping (Fig.S6(b)) photodetectors. The curves represent the plane wave normal to the surface for the E component of the EM field parallel to the metal fingers vs. the perpendicular and the averaged value. A very low absorption loss has been observed due to the interdigitated metal in photon-trapping devices compared to the planar devices.

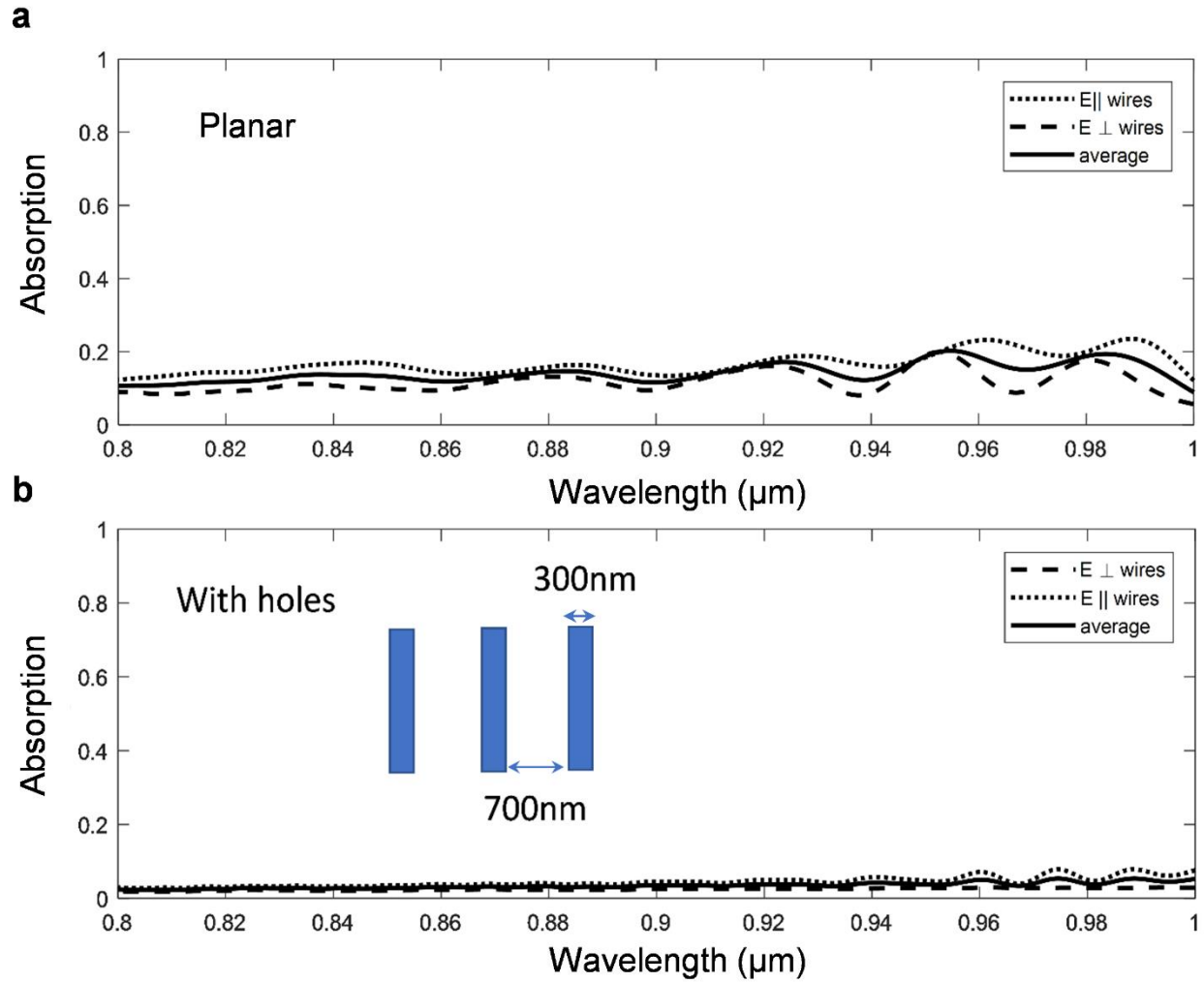


Figure S6: **Optical absorption of the aluminum interdigitated metals.** (a) Optical absorption of Al interdigitated metals in planar Si MSM photodetector, (b) Extremely low optical absorption of Al interdigitated metals in photon trapping Si MSM photodetectors.

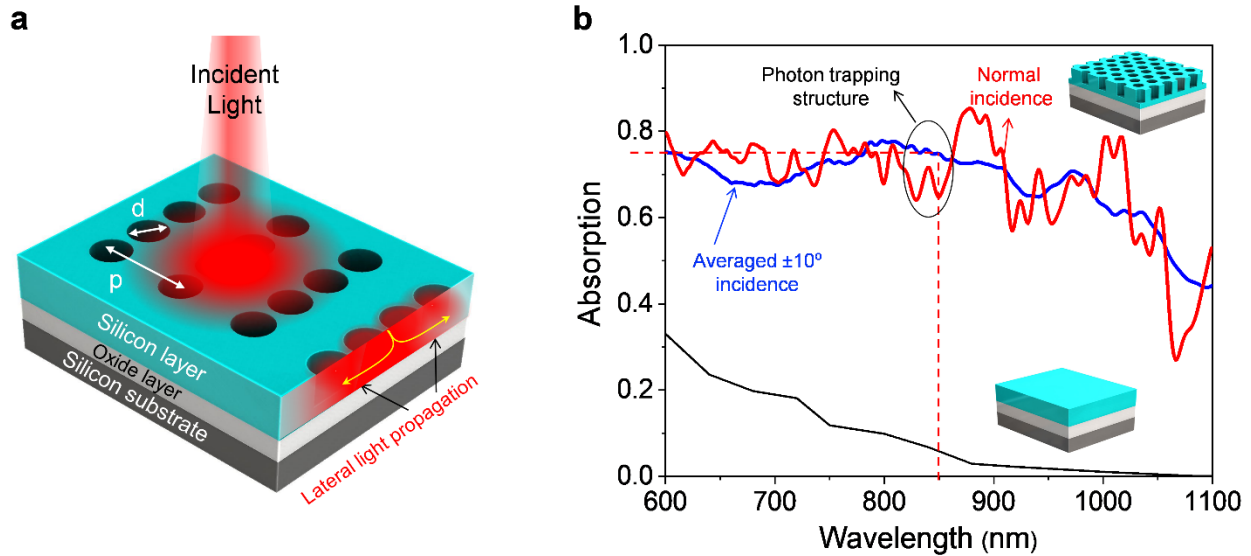


Figure S7: Optical absorption in photon-trapping silicon photodetectors under normally incident illumination and incident light with different angles (a) Schematic of silicon slab on silicon-on-insulator (SOI) integrated with cylindrical photon-trapping holes that allow lateral propagation of light resulting in enhanced optical path length and photon absorption, where (p) is the periodicity of the photon-trapping array, and (d) is the photon-trapping hole diameter, (b) A comparison of simulated absorption of photon-trapping and planar (flat) Si MSM photodetectors, where red and blue curves are simulated absorption spectra for normally incident light and averaged among $\pm 10^\circ$ angles, respectively.

The cross-sectional simulation structure is schematically shown in Fig. S6 (a). A thin Si absorber is assumed to be prepared on an SOI substrate. The photon-trapping photodetector is simulated for absorptions in wavelengths ranging from 600 nm to 1100 nm as presented in Fig. S6 (b). A photodetector with a planar surface is also simulated as a reference. The red and blue curves are simulated absorption spectra of photon-trapping photodetectors for normally incident light and incident light averaged between $\pm 10^\circ$ angles, respectively. The photon-trapping photodetectors exhibit distinctly higher absorption in comparison with the planar counterpart. For devices with

photon-trapping structures and the normally incident light illumination, a maximum photon absorption exceeding 85% is achieved around 880 nm wavelength. We also observe that the simulated devices exhibit photon absorption beyond $4n^2$ (n is the refractive index of the silicon material as a function of incident wavelength) in the wavelength spectrum ranging from 820 nm to 1100 nm as can be seen. Moreover, the maximum absorption enhancement can be as high as $27n^2$ by integrating our fabricated devices' most optimized photon-trapping holes. The corresponding calculated responsivities of the characterized devices are also depicted in Fig. S7 for a broad wavelength spectrum.

We have attached a numerical simulation showing the optical absorption in an optimized square lattice pattern with circular holes and compared it with a hexagonal lattice pattern with circular holes. Photon-trapping holes arranged in hexagonal lattice show higher optical coupling performance than the square lattice, as depicted in Fig. S8, since the incident light couples more efficiently in such a design, resulting in enhanced optical path length and light-matter interactions.

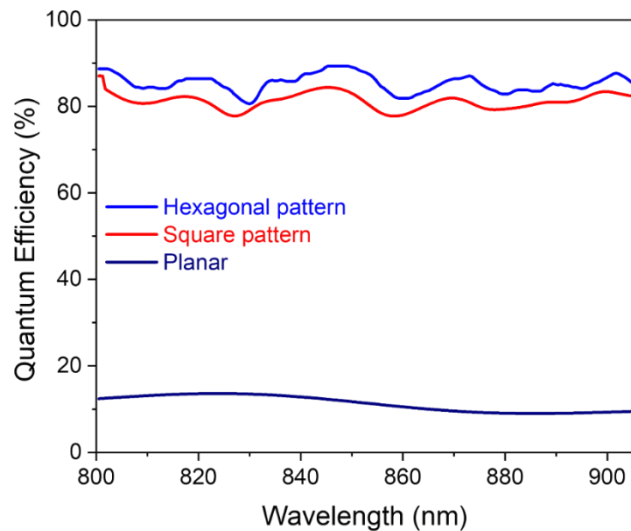


Figure S8: Comparison of calculated quantum efficiency between planar and photon-trapping silicon photodetectors with hexagonal and square patterns.

Then the influence of different microhole shapes/channels on the quantum efficiency of 1.0-micrometer thick silicon photon-trapping photodetectors has been studied, as presented in Fig. S9. It should be mentioned here that the simulations are performed based on a single micromole, and the devices are not optimized. The goal was to justify that different shapes would impact light-matter interaction differently.

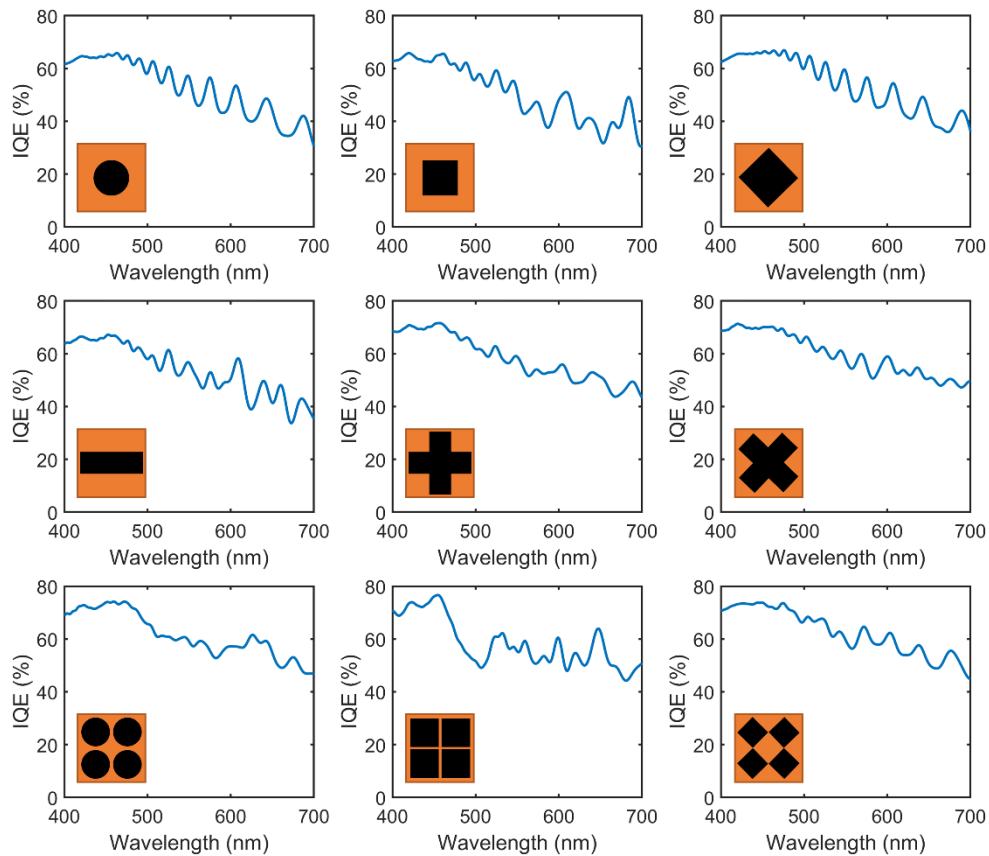


Figure S9: Comparison of calculated quantum efficiency with varying photon-trapping hole shapes. The devices are studied based on a single hole and are not optimized.

The measured dark current characteristics of a 50 μm planar and photon-trapping photodetectors are presented in Fig. S10. The planar device exhibits 67 nA dark current at 3V biasing, whereas the photon-trapping pronounces 157 nA.

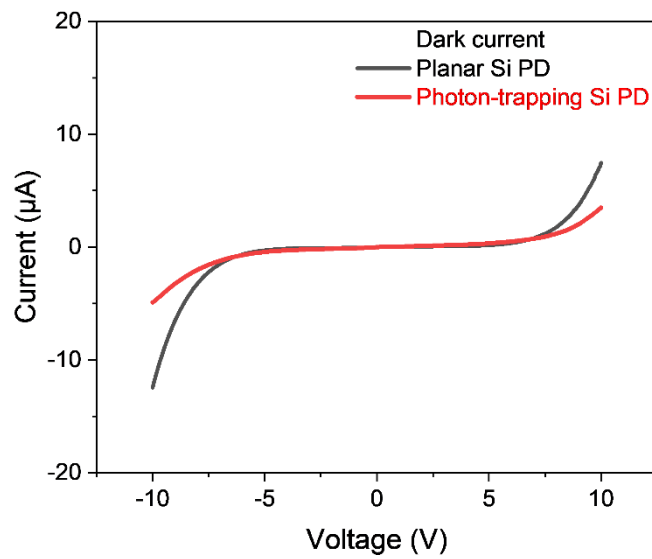


Figure S10: Dark current characteristics of the fabricated 50 μm planar and photon-trapping photodetectors.

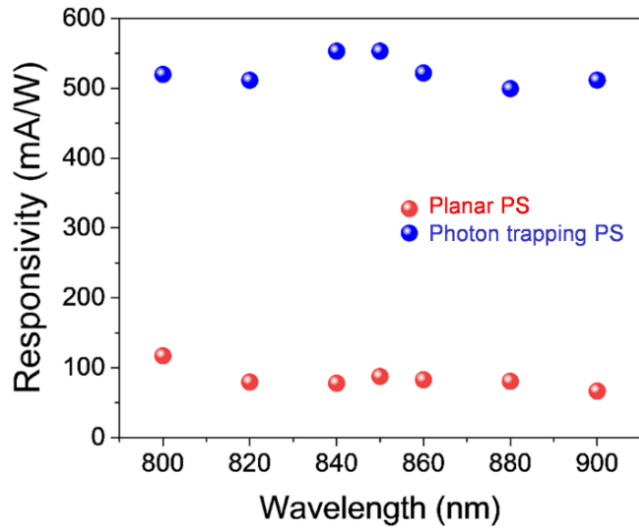


Figure S11: **Responsivity of the fabricated photodetectors.** The measured responsivity of the fabricated control and photon-trapping photodetectors. The periodicity (p) and diameter of the photon-trapping structures are 1300 and 1000 nm, respectively, while the device's active layer thickness (t_{Si}) is 1000 nm.

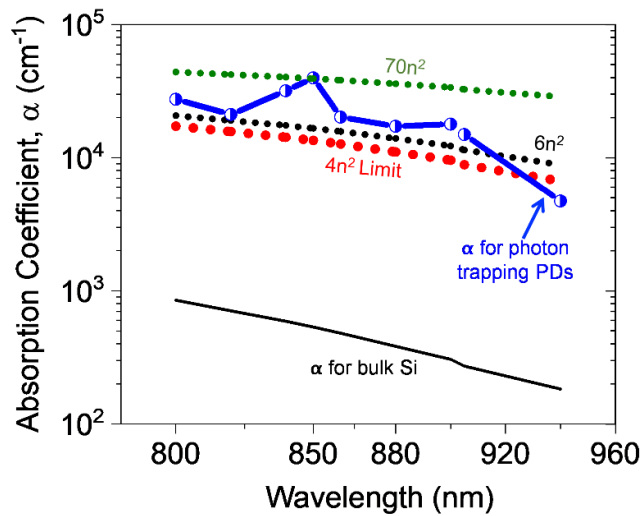


Figure S12: **Excellent enhanced absorption coefficient obtained from the fabricated photon-trapping photodetectors.** The maximum enhanced absorption coefficient obtained from the most optimized fabricated photon-trapping photodetectors exceeded $70n^2$, where n is the refractive

index of the material. The devices were measured by a collimated beam, which does not allow to directly compare this absorption coefficient with the geometrical light-trapping limit of $4n^2$.

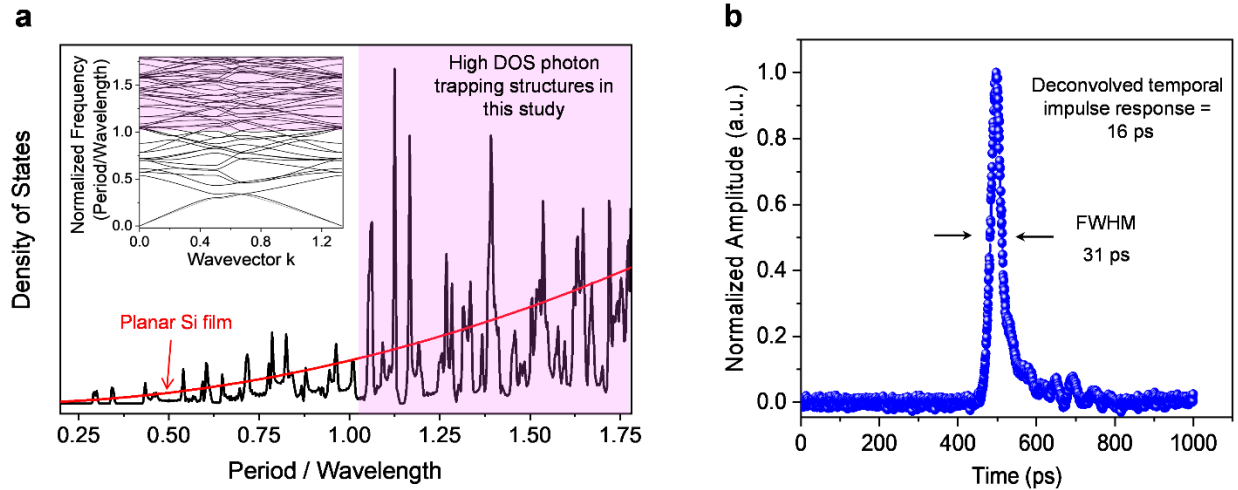


Figure S13: **High density of states and ultrafast time response of photon-trapping photodetectors.** (a) Normalized energy band structure of photon-trapping photodetectors with a hole diameter and period ratio (d/p) of 0.7 (inset) and the corresponding density of states (DOS), where high peaks in the DOS are observed for frequency (period/wavelength) points higher than 1.0 (shaded region). The red line shows the DOS for the planar devices. (b) The 1000 nm thin fabricated MSM photodetector exhibits an ultra-fast time response of 31 ps in full width at half maximum (FWHM). The actual time response of the device is approximated to be ~ 16 ps by considering 22 ps and 15 ps FWHM response for the 20 GHz sampling oscilloscope and optical laser pulse width, respectively.

3. Ultrafast response measurement:

The high-speed characterizations of the fabricated metal-semiconductor-metal photodetectors were performed by an approx. 15 ps pulse width pulsed laser with a repetition rate and incident wavelength of 70 MHz and 850 nm, respectively, on a microwave probe station. The photocurrent

of the tested photodetectors with a 50 μm diameter was maximized by aligning the center of the optical light beam with a translational stage, while the active region was mainly targeted to be hit by the pulse of the single-mode fiber tip on the probe stage. The input and output power were set at around 1 mW and 100 μW , respectively. In this case, a 20 GHz sampling oscilloscope was utilized to observe the resulting photoresponse of the photodetectors as the electrical pulses, while a 25 GHz bias-T was used for the DC biasing of the photodetectors.

The high-speed pulse response of a photon-trapping photodetector is depicted in Fig. S9 (b) for the incident wavelength of 850 nm. The full width at half maximum (FWHM) for the photon-trapping Si photodetectors is measured to be ~ 31 ps. However, the actual time response of the device is approximated to be ~ 16 ps by considering 22 ps and 15 ps FWHM response for the 20 GHz sampling oscilloscope and optical laser pulse width, respectively, which is a valid approximation for our actual measurement with Gaussian pulses.

4. A physics-based explanation for the performance enhancement

We investigated the energy band structure and the corresponding density of states of the photon-trapping photodetector as shown in Fig. S9 (a). The optical density of states (DOS) influences photon absorption in optoelectronic devices. Herein, the ratio of hole diameter and period of the photon-trapping photodetectors is assumed to be $d/p \approx 0.7$, which is consistent with the fabricated devices. The frequency of the energy band diagram was normalized by $2\pi c/p$ so that the values represent period/wavelength, where c and p are the light velocity and the lattice period, respectively. Furthermore, the wavevector is also normalized by $2\pi/p$. The density of states is calculated as an integral over the wavevector for a given frequency. DOS for photodetectors with planar surfaces (without nanoholes) is also added to Fig. S9 (a) as a reference (red curve). First,

the DOS of the photon-trapping photodetectors is found to be higher than that of the photodetectors with planar (flat) surfaces. Then the photodetectors with nanohole periods shorter than the incident wavelengths exhibit distinctly low DOS as compared to the periods which are comparable and/or slightly longer than the wavelengths. For instance, the photonic DOS for a nanohole period of 450 nm and an incident wavelength of 850 nm ($p/\lambda \sim 0.53$) is determined to be distinctly poor. However, our designed and fabricated devices match more with the shaded area on the right part, exhibiting high DOS for the frequency points higher than 1.0 (periods are comparable to and/or slightly longer than the incident wavelengths). Nevertheless, the region with high values of p/λ needs more Fourier components, and the maximum peaks of the DOS are not as pronounced as expected, while there is a constant increase of the optical mode density with p/λ .

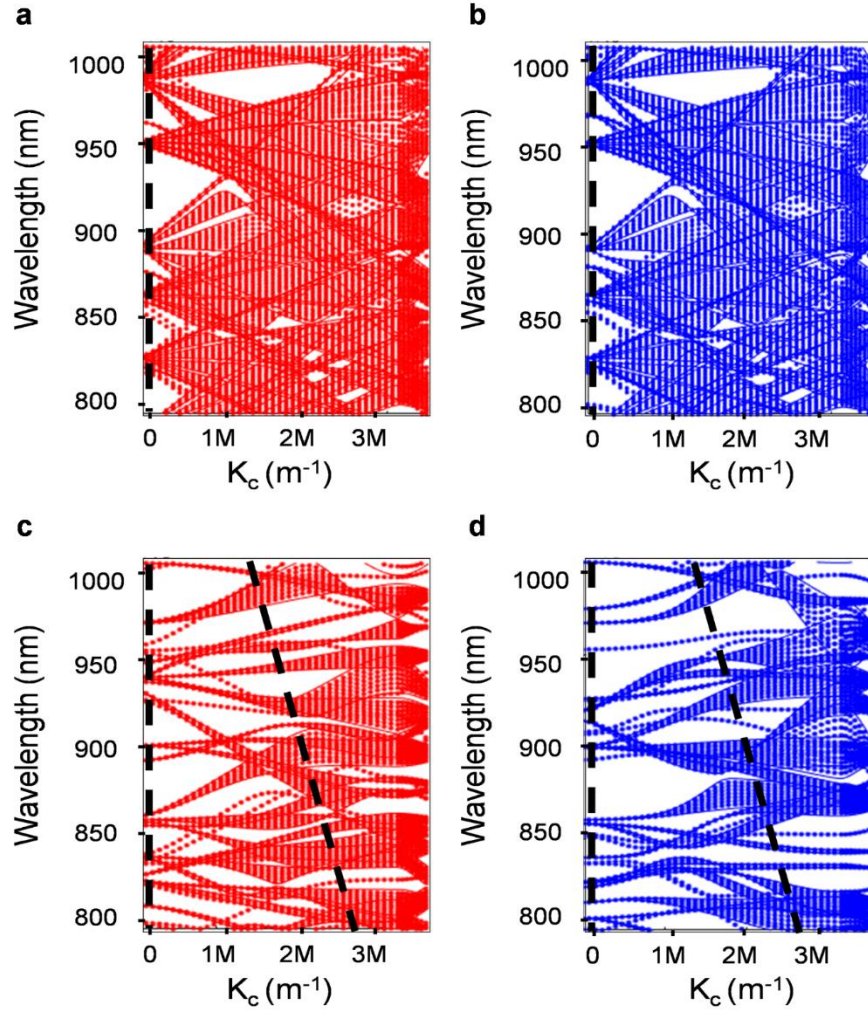


Figure S14: **Simulated band structure of photon-trapping silicon structures.** (a) Band structure for photon-trapping structure with a diameter (d) = 100 nm, periodicity (p) = 1000 nm, Si thickness (t_{Si}) = 1000 nm, TE polarization, (b) Band structure for photon-trapping structure with diameter = 100 nm, periodicity = 1000 nm, thickness = 1000 nm, TM polarization, (c) Band structure for photon-trapping structure with diameter = 700 nm, periodicity = 1000 nm, thickness = 1000 nm, TE polarization, (d) Band structure for photon-trapping structure with diameter = 700 nm, periodicity = 1000 nm, thickness = 1000 nm, TM polarization. Slanted dash lines are solutions for k_c that couple into the lateral propagation for a vertically illuminating light source. Small holey structures exhibit solutions only for the finite number of the eigenmodes with $k=0$ (vertical dashed

line), while large holey structures essentially have both solutions $k=k_c$ and $k=0$ (vertical and slanted dash lines) with the eigenmodes, pronouncing enhanced coupling phenomena and laterally propagated optical modes.

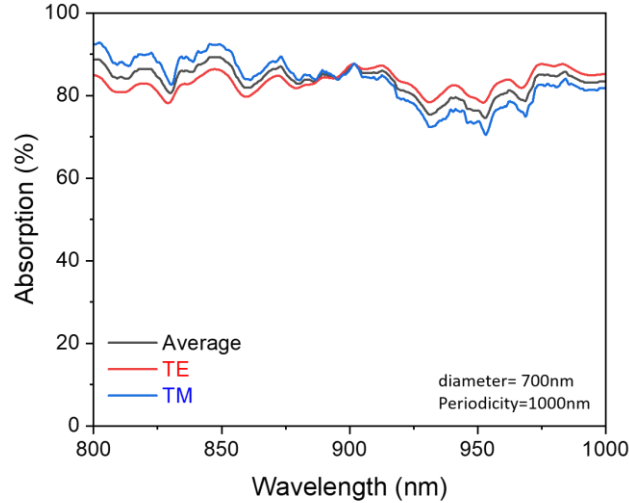


Figure S15: Simulated absorption plots of one-micrometer-thick photon-trapping silicon under TM and TE polarizations. The diameter and periodicity of the microholes were chosen as 700 nm and 1000 nm, respectively.

While the band diagram provides the eigenmodes in the lateral propagation, the coupling from the vertical incidence into the lateral could be described in the model of coupling the light into one hole. The holes have a size comparable with the incident wavelengths and the light forms the modes inside each hole. The FDTD simulations show that the light couples into the hole and leaks into Si, as shown in Fig. S11 (b). The field in each hole could be described as a propagation along the hole with complex wave vector β and lateral wave vector $q_l^2 = (n_1 k_0)^2 - \beta^2$ inside the hole with

$n_1 = 1$ for air and $k_0 = 2\pi/\lambda$ and $q_2^2 = (n_2 k_0)^2 - \beta^2$ outside the hole where n_2 is the complex refractive index of Si.

The condition for the optical coupling into the eigenmodes of the array can be derived from the conditions when the eigenmode of the hole array $k = q_2$. When the diameter of the holes is small, we will have one possibility of light coupling for the vertical incidence where k is very small or $k = 0$; this happens when the incidence light is nearly vertical. As we can see in Figs. S10 (a-b), there are not many eigenmodes for the coupling. However, if the hole size is comparable to the incident wavelength, the light can couple into the holes and leak out through the sidewalls of the holes, as we can see in Figs. S10 (c-d). In the case of the hole diameter being considerably smaller than the incident wavelength, there is no light coupling into the holes.

The large diameter holes (hole diameter is comparable to the incident wavelength) result in the light leaking laterally into the Si between the holes. From the boundary conditions, it will be possible only if β inside the hole and outside the hole are equal. The conditions when the significant lateral field component will be produced can be found in the cylindrical coordinates for a hole with radius a , and k_0 is the wave vector for a given frequency in a vacuum, n , and ϵ are the refractive index, and dielectric constant of the Si, respectively.

To find the solution for the single hole, we solve Maxwell's equations for the field in the cylindrical coordinates r , θ , and z along the hole axis in the form:

$$E = R(r)\Theta(\theta)e^{-i\beta z} \quad (\text{S1})$$

In this case, the wave equation is:

$$\frac{\partial^2 E_z}{\partial r^2} + \frac{1}{r} \frac{\partial E_z}{\partial r} + \frac{1}{r^2} \frac{\partial^2 E_z}{\partial \theta^2} + (k^2 n(r, \theta)^2 - \beta^2) E_z = 0 \quad (\text{S2})$$

The intensity along the hole decays and it is described by the imaginary part of β . The solution inside and outside the hole is the Bessel function. The solution outside the hole is also described by the Bessel functions of the first kind with complex q_2 that takes into account the absorption in Si. In the case when the absorption of the Si is small, only the real part of q_2 can be considered.

As one can see from the FDTD simulations Fig. S11 it is not evanescent as it is for the field approximation in an optical fiber. Matching the boundary conditions at the boundary of the hole, we have the following dispersion equation:

$$\left(\frac{J'_n(q_1 a)}{q_1 J_n(q_1 a)} + \frac{J'_n(q_2 a)}{q_2 J_n(q_2 a)} \right) \left(\frac{k_0^2 J'_n(q_1 a)}{q_1 J_n(q_1 a)} + \frac{\epsilon k_0^2 J'_n(q_2 a)}{q_2 J_n(q_2 a)} \right) = \left(\frac{\beta n}{a} \right)^2 \left(\frac{1}{q_1^2} + \frac{1}{q_2^2} \right)^2 \quad (\text{S3})$$

$$k_0 = \frac{2\pi}{\lambda}, \quad q_1^2 = k_0^2 - \beta^2, \quad q_2^2 = \epsilon k_0^2 - \beta^2 \quad (\text{S4})$$

Where J is the first kind of Bessel function. The solution $q_2 = k_c$ of the equation provides us with the lateral wave vectors in Si that are coupled with eigenmodes. The crossing points of the solution $k = k_c$ or $k = 0$ with the eigenmodes give us the modes that propagate laterally and have been absorbed in the Si. For the small diameter holes, we have the solutions only for the finite number of the eigenmodes with $k = 0$, which corresponds to the guided modes in photonic crystals. They produce sharp spikes in absorption, as shown in Fig. (4d). In the case of the large-diameter holes, there is a continuous solution for any wavelength in the range of interest between 0.8 and 1 μm . In addition to that, they have small group velocity u_g that also increases the absorption with more extended light-matter interaction.

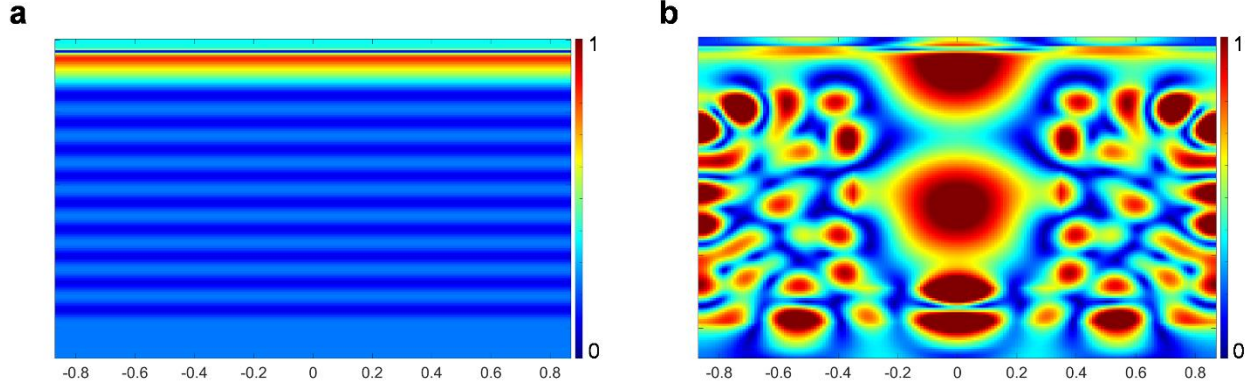


Figure S16: **Electromagnetic field distribution mapping in planar and holey photon-trapping structure.** FDTD optical simulation for light coupling in (a) Planar and (b) Photon-trapping Si photodetector on SOI.

Table. S1: **Performance comparison of high-speed silicon photodiodes for optical communications.** Photo sensitivities or quantum efficiencies and approximated bandwidth of the fabricated photodetectors for a broadband spectrum in the near-infrared are also included as a comparison.

Ref.	Device type	Responsivity (A/W) or EQE	Wavelength (nm)	Bandwidth (GHz) or data rate (Gb/s)	CMOS compatibility and other challenges
Si[44]	p ⁺ -p-n avalanche	0.74 A/W (at 823 nm)	850	1.6 GHz, 3.5 Gb/s	0.18 μm CMOS technology
Si [60]	p ⁺ -n-p	N.A.	850	3 Gb/s with an analog equalizer	0.18 μm CMOS technology
Si [61]	Resonant cavity <i>pin</i>	40 % EQE	860	10 Gb/s	Complex cavity mirror fabrication
Si [62]	Resonant cavity <i>pin</i>	40 % EQE	822	10 GHz, >10 Gb/s	Complex cavity mirror fabrication
Si [63]	MSM	N.A.	850	2.5 GHz	CMOS compatible

Si [64]	lateral <i>pin</i>	47% internal QE	840	NA.	CMOS compatible
Si[65]	lateral <i>pin</i>	0.32 A/W (from 4 PDs)	850	10 Gb/s with TIA	0.13 μm CMOS technology
Si [66]	vertical <i>pin</i>	0.26 A/W	850	Could be 11 Gb/s with equalizer	Modified 0.5 μm BiCMOS technology
Si [67]	vertical <i>pin</i>	52% EQE at 850 nm	broadband absorption between 800-900 nm	>10 GHz	CMOS compatible
Si [68]	APD	0.07 A/W	850	5 GHz, 12.5 Gb/s with equalizer circuit	0.25 μm Si/Ge BiCMOS technology
Si [68]	APD	10% EQE	850	8 Gb/s	0.13 μm CMOS technology
Si[69]	APD (double PD)	0.84 A/W	850	0.7 GHz	40 nm CMOS technology
Si[70]	Spatially-modulated APD	0.18 A/W	850	8 GHz, 12.5 Gb/s with TIA, equalizer and limiting amplifier	0.13 μm CMOS technology
Si[71]	APD	4.67 A/W	850	10 Gb/s	0.13 μm CMOS technology
Si[72]	APD	2.94 A/W	850	3.2 GHz	65 nm CMOS technology
Si[73]	SPAD	PDP <10% at 850 nm	850	Sub-40ps gate shifts	Standard CMOS technology
Si[74]	SPAD	PDP <5% at 850 nm	850	160 ps FWHM	0.35 μm CMOS technology
Si[75]	Lateral PIN	36.8% (theoretical 77%)	850	11.3 GHz	
Si-Ge[76]	PIN	-	1550	60 GHz	16 nm CMOS technology
Graphene-Si [77]	Graphene PIN	35 mA/W (~70% visible)		65 GHz (3-dB cutoff)	CMOS compatible

Nano-structured Si [48]	SPAD	32% PDE*	850	25 ps (FWHM)	CMOS compatible
Si [This work]	MSM	86% EQE at 850 nm (1 μm thin Si)	broadband absorption between 800-940 nm	>16 GHz Ultimate BW (50 μm device)	CMOS compatible (Monolithic Integration)
Si [This work]	MSM	72% EQE at 905 nm (1 μm thin Si)	broadband absorption between 800-940 nm	>16 GHz Ultimate BW (50 μm device)	CMOS compatible (Monolithic Integration)
Si [This work]	MSM	32% EQE at 940 nm (1 μm thin Si)	broadband absorption between 800-940 nm	>16 GHz Ultimate BW (50 μm device)	CMOS compatible (Monolithic Integration)

Movie S1: Demonstration of bending normally incident beams of light by almost ninety degrees and transformed into laterally propagating modes of light along the plane of the silicon film integrated with engineered an array of periodic photon-trapping structures. Such surface structures effectively increase the propagation length of light, contributing to more than an order of magnitude improvement in light absorption efficiency in photodetectors.

Movie S2: Propagation of light in both silicon planar (left) and photon-trapping (right) photodetectors for the incident wavelength of 850 nm. Most of the light incident on the planar device either reflects from the surface or passes through it and cannot efficiently absorb in the silicon, whereas light incident on the photon-trapping structures bends almost at a right angle into laterally propagating modes of light along the plane of the Si absorber layer. The photon-trapping surface structure reduces the surface reflection, enhances the confinement of light within the silicon absorber layer, and increases the light-matter interaction. Such photon-trapping structure in one-micron silicon facilitates very high photoabsorption as well as ultrafast time response.

Movie S3: Optical propagation of light in 30 nm ultra-thin silicon with integrated photon-trapping structure. Similar to the Si film with 1000 nm thickness, photon-trapping ultra-thin Si film exhibits dramatically higher absorption efficiency than the planar Si film. More than 8% absorption efficiency can be obtained, while it is less than 1% in such planar silicon. Such ultrathin Si-based photo-trapping-equipped photodetectors are intriguingly encouraging for the fabrication of ultrafast photodetectors in the existing CMOS foundry framework.